# Day-to-day ionospheric variability due to lower atmosphere perturbations

H.-L. Liu,[1] V. A. Yudin,[2] and R. G. Roble[1]

Received 3 December 2012; revised 21 December 2012; accepted 24 December 2012; published 27 February 2013.

[1] Ionospheric day-to-day variability is a ubiquitous feature, even in the absence of appreciable geomagnetic activities. Although meteorological perturbations have been recognized as an important source of the variability, it is not well represented in previous modeling studies and the mechanism is not well understood. This study demonstrates that the thermosphere-ionosphere-mesosphere-electrodynamics general circulation model (TIME-GCM) constrained in the stratosphere and mesosphere by the hourly whole atmosphere community climate model (WACCM) simulations is capable of reproducing observed features of day-to-day variability in the thermosphere-ionosphere. Realistic weather patterns in the lower atmosphere in WACCM were specified by Modern Era Retrospective Reanalysis for Research and Application (MERRA). The day-to-day variations in mean zonal wind, migrating and nonmigrating tides in the thermosphere, vertical and zonal $E \times B$ drifts, and ionosphere F2 layer peak electron density (NmF2) are examined. The standard deviations of the drifts and NmF2 show local time and longitudinal dependence that compare favorably with observations. Their magnitudes are 50% or more of those from observations. The day-to-day thermosphere and ionosphere variability in the model is primarily caused by the perturbations originated in lower atmosphere, since the model simulation is under constant solar minimum and low geomagnetic conditions. **Citation:** Liu, H.-L., V. A. Yudin, and R. G. Roble (2013), Day-to-day ionospheric variability due to lower atmosphere perturbations, *Geophys. Res. Lett.*, *40*, 665–670, doi:10.1002/grl.50125.

## 1. Introduction

[2] Day-to-day variability is one of the key features of a weather system, be it a terrestrial weather system or a space weather system. Understanding and quantifying the causes of the variability is of essential importance for studying the predictability of such a system. The ionosphere and thermosphere (IT), as the main components of the space weather system, is subject to strong radiative and particulate forcing from the Sun and the magnetosphere, and to perturbations from the lower atmosphere (LA). Therefore, the predictability of a space weather system entails understanding and quantifying the interactions of this system with different types of forcing from below and above. According to *Rishbeth and Mendillo* [2001], geomagnetic activity and perturbations from the LA contribute comparably to the day-to-day F2 region variability. The most likely pathway that the LA perturbations affect the IT system is through atmospheric waves, including tides, planetary waves, and gravity waves. The wave-induced variations in the IT can change from day to day due to the variability of wave sources, propagation conditions, and nonlinear wave-wave interactions. The LA wave impacts are exemplified by the satellite observations of nonmigrating tidal signature in equatorial ionosphere anomaly (EIA) [*Sagawa et al*., 2005; *Immel et al*., 2006] and IT changes during stratospheric sudden warming (SSW) [e.g., *Chau et al*., 2012, and references therein].

[3] To study the LA impact on the upper atmosphere in a self-consistent way is the major motivation for the recent development of whole atmosphere models [*Akmaev*, 2011]. Using the NCAR whole atmosphere community climate model (WACCM), *Liu et al*. [2009] explored the predictability of the upper atmosphere characterized by model error growth and found that it is closely tied to waves originated in LA. As demonstrated there, accurate specification of the LA state, including atmospheric waves, effectively limits the error growth and increases the predictability of the upper atmosphere. More recently, whole atmosphere simulations of the 2009 SSW were able to produce significant ionospheric day-to-day variability [*Fuller-Rowell et al*., 2011; *Jin et al*., 2012]. The meteorological impacts on the IT system have also been studied by the thermosphere-ionosphere-mesosphere-electrodynamics general circulation model (TIME-GCM) [*Roble*, 2000, and references therein], using meteorological specification at the model lower boundary, but the IT variability from the simulations is weak compared with observations. This is probably because (1) the intrinsic inconsistency between the meteorological forcing (reanalysis or operational data) and TIME-GCM leads to degradation of model results, and (2) the low-frequency output of standard reanalysis/operational data (at best 6-hourly) hinders the model capability of resolving tides and tidal variability, which plays a key role in IT variability. The goal of this study is to develop a numerical scheme so that the model could be more effectively driven by realistic LA forcing and to study the corresponding IT variability.

## 2. Constraining TIME-GCM with WACCM-X/MERRA Simulations

[4] **TIME-GCM**. TIME-GCM is a time-dependent, three-dimensional model that solves the nonlinear hydrostatic equation of the neutral gas from the upper stratosphere (10 hPa) to the thermosphere ($4.6 \times 10^{-10}$ hPa). This

[1]High Altitude Observatory, National Center for Atmospheric Research, Boulder, Colorado, USA.
[2]Atmospheric Chemistry Division, National Center for Atmospheric Research, Boulder, Colorado, USA.

Corresponding author: H.-L. Liu, High Altitude Observatory, National Center for Atmospheric Research, P.O. Box 3000, Boulder, CO 80307-3000, USA. (liuh@ucar.edu)


0094-8276/13/10.1002/grl.50125

model simulates self-consistently the coupling between the thermosphere and ionosphere, including electrodynamics driven by the neutral thermodynamics [*Richmond et al*., 1992]. The spatial resolution of the TIME-GCM used here is 2.5° × 2.5° in the horizontal direction and quarter scale height in the vertical. In standard TIME-GCM configuration, daily fields from reanalyses and climatological tides are introduced through the lower boundary conditions at 10 hPa. Details of the model and comparison of model results with observations can be found in *Roble* [2000, and references therein]). With this setup, however, day-to-day tidal variability caused by changes of wave sources and mean flow below 10 hPa cannot be accounted for. This restricts the model capability for studying short-term variability in the IT region. Our previous numerical experiments also show that the stratosphere-mesosphere state of TIME-GCM does not always agree quantitatively with the reanalysis results above 10 hPa.

[5] To address these limitations of TIME-GCM and constrain the neutral dynamics below the mesopause, a one-way coupling between WACCM-X and TIME-GCM is performed in this study through relaxation of TIME-GCM temperature and horizontal winds to the hourly WACCM-X simulations. The relaxation is strongest at the lower boundary of TIME-GCM, where WACCM-X winds and temperature overwrite the TIME-GCM model fields, and is gradually reduced to zero at ~95 km. Constraining TIME-GCM up to the mesopause will help to reduce deviation between dynamics of the two models caused by the differences in parameterized gravity wave forcing (strongest in the mesosphere) and at the same time retain the model capability of self-consistently resolving the ion-neutral coupling in E and F regions. It should be emphasized that the simulations are under a constant solar minimum condition (f10.7 cm flux set to 70 sfu), and quiet geomagnetic condition, with the hemispheric power, cross polar cap electric potential and the southward component of the interplanetary magnetic field $B_z$ set to 8 GW, 30 kV, and 0, respectively. Therefore, the ionospheric day-to-day variability from the model is caused solely by the variability introduced by LA perturbations.

[6] **WACCM-X/MERRA**. The thermosphere extension of WACCM (WACCM-X) is described in detail by *Liu et al*. [2010]. As a climate model, the free-running WACCM-X does not reflect variability pertaining to a specific year. A framework that can address this issue is constraining the LA in WACCM-X with meteorological analyses performed by the numerical weather prediction systems. This was done in this study by using the meteorology of MERRA reanalysis [*Rienecker et al*., 2011] for January–February 2006, which was under solar minimum conditions and was a period with a stratospheric warming event. The hourly WACCM-X/MERRA results properly represent the broad spectra of tides, allowing an accurate and self-consistent representation of their diurnal and subdiurnal variations as well as the background flow. The TIME-GCM is relaxed to these hourly results as discussed earlier in this section.

## 3. Model Results

[7] We first examine the variability of the neutral atmosphere in the simulation, in terms of mean and tidal winds. Figure 1a shows the zonal mean zonal winds in the winter stratosphere (60°N) and equatorial lower thermosphere and upper thermosphere from the simulation. Within the altitude range where TIME-GCM is constrained, the TIME-GCM results are very close to WACCM-X/MERRA. The wind and temperature changes during the major SSW event, which peaks around January 26, 2006, and undergoes a gradual recovery afterward, are accurately represented. At $10^{-4}$ hPa (~105 km), where the neutral circulation is solved by TIME-GCM without any explicit constraint, the equatorial zonal wind changes significantly on similar timescales. On day-to-day scales, the zonal wind at this altitude display quite large variability (10–20 $ms^{-1}$) throughout the simulation period. At upper thermosphere (around the F2 peak altitude), the zonal wind also shows variation on SSW timescales somewhat similar to the lower thermosphere wind but with a smaller magnitude, as well as day-to-day variability.

[8] Both migrating and nonmigrating tides display large variability, especially in the lower thermosphere. This is evident by comparing the standard deviation and mean of the tidal amplitudes over the simulation period in Figure 1b and c. For migrating diurnal and semidiurnal tides (DW1 and SW2), the standard deviations are about 50% and 25% of the mean values at their respective peak latitudes. As for the two nonmigrating components, the diurnal eastward propagating wave 2 (DE2) is stronger than wave 3 (DE3) for this time of the year and the standard deviations are both ~50% of their respective maximum amplitudes at the equator. Although some of the variability is probably caused by SSW, the large day-to-day tidal variability from WACCM-X simulations persists throughout the year and is a ubiquitous feature in the upper atmosphere [*Liu*, 2013]. They are likely caused by the wind variability (Figure 1a), which affects the tidal propagation condition, as well as variability of wave sources and interactions between waves.

[9] Figure 2 shows the vertical and zonal components of the $E \times B$ drift (vertical and zonal drifts hereafter) and their variabilities near the geomagnetic equator at 75°W. The mean vertical drift over the simulation period reaches a maximum upward value (25 $ms^{-1}$) at LT1000 and strong downward values at LT0400 and LT1700 (–55 and –15 $ms^{-1}$, respectively). The scattering around the mean over the simulation period is ±10–20 $ms^{-1}$ at most local times, although it is larger around LT0300 and 2200. The standard deviation has a clear local time dependence, with the maximum values (~10 $ms^{-1}$) around LT0300 and LT1800 and minimum (~4 $ms^{-1}$) around local noon. From the daily values of the vertical drift at LT0500 (dotted), LT1000 (solid), and LT1900 (dashed), it is seen that the day-to-day variation can be as large as 10–20 $ms^{-1}$ (larger at LT0500 and LT1900). Under the constant solar minimum conditions, the presence of pre-reversal enhancement (PRE) varies day by day, although the mean vertical drift does not show a clear PRE.

[10] The mean zonal drift is westward from LT0500 to LT1700 and eastward at other local times. The maximum westward drift (–50 $ms^{-1}$) occurs at LT1000, and the eastward drift reaches maximum (50 $ms^{-1}$) at LT2000 and a secondary maximum at LT0300 (30 $ms^{-1}$). The scattering around the mean is ±20–50 $ms^{-1}$, with the largest scattering occurring between LT1900 and LT0500. This local time dependence is seen from the standard deviation: it has a maximum of 24 $ms^{-1}$ at LT0200 and a secondary maximum of 18 $ms^{-1}$ at LT2100, and it stays at 10 $ms^{-1}$

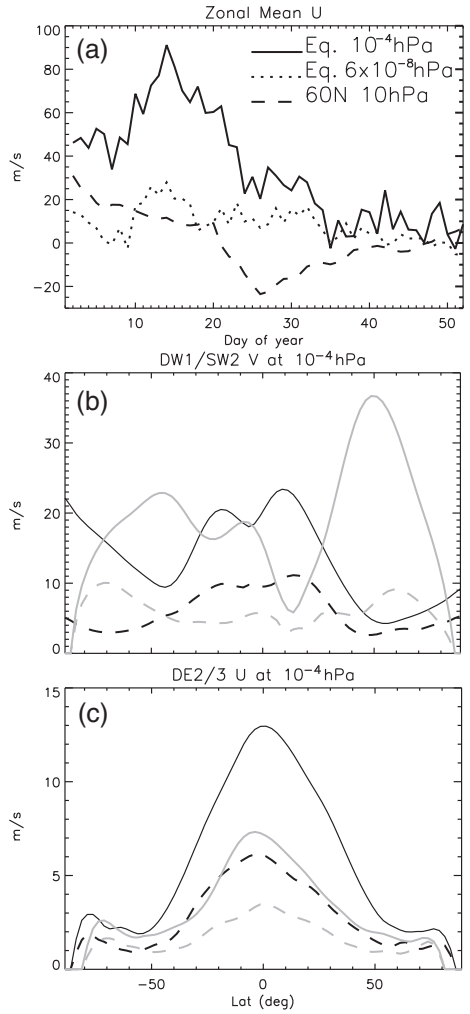


**Figure 1.** (a) Mean zonal wind at $10^{-4}$ hPa (~105 km) and the equator (solid), $6\times10^{-8}$ hPa (~250 km) and the equator (dotted), and 10 hPa (~30 km) and 60°N (dashed). (b) Mean amplitudes (solid) and standard deviations (dashed) of the meridional wind component of DW1 (black) and SW2 (gray) over the simulation period at $10^{-4}$ hPa. (c) Similar to (b), but for the zonal wind component of DE2 (black) and DE3 (gray).

during the day (between LT0500 and LT1700). Like the vertical drift, the zonal drift also displays large day-to-day variation, with typical values between 10 and 30 $ms^{-1}$ (Figure 2d). Consistent changes for several consecutive days are seen between January 5 and 25, which could be related to SSW.

[11] We compare these model results to measurements and climatological values at the Jicamarca Radio Observatory (JRO) (~12.0°S, 76.9°W) for November–February under solar minimum and geomagnetically unperturbed conditions [*Scherliess and Fejer*, 1999; *Fejer et al*., 2005, for vertical drift and zonal drift, respectively]. For the vertical drift, it is seen that the model captures the times when it reaches the largest downward value (LT0400), when it changes from downward to upward (at LT0600), when the upward drift peaks (LT1000), and when the afternoon drift reaches minimum (LT1700). The maximum upward drift at LT1000 from the model is also in good agreement with the observations. On the other hand, the model seems to overestimate the downward drifts around LT0400 and in the afternoon, and the transition from upward to down drift occurs 3 h later than the observation (LT2300 versus LT2000). Both could result from a weak SW2 in the model. For the zonal drift, the model results generally compare well with observations during the daytime (LT0500–LT1700) when the drift is westward, including the magnitude and timing of the maximum westward drift. The observed eastward drift at night, however, is much stronger than the model results and reaches the maximum (100 $ms^{-1}$) 1 to 2 h later than that in the model. Probably because of the large nighttime eastward drift, the observed eastward drift does not display any secondary maximum after midnight, although it does have a turning point at ~LT0400.

[12] A remarkable feature from the constrained model simulations is that the vertical and zonal drifts display short-term variability similar to observations. As mentioned earlier, the scattering from the daily plots of vertical drift (Figure 2a, a proxy to day-to-day variability) is $\pm$10–20 $ms^{-1}$ around the mean value. This is in good agreement with the scattering from vertical drift observations over JRO under solar minimum and geomagnetically quiet conditions (Figure 1 in *Scherliess and Fejer* [1999]). Its standard deviation of ~5 $ms^{-1}$ and day-to-day change of up to ~15 $ms^{-1}$ during the day are in good agreement with those obtained by *Fejer and Scherliess* [2001] from observations. The standard deviation of zonal drift from the model shows a local time dependence that is similar to that measured over JRO (Figure 3 in *Fejer et al*. [2005])—relatively small during the day and larger in the evening and early morning. Quantitatively, however, the standard deviation of the zonal drift from the model is about half of that from observations. It is worth noting that the longer time coverage of the observations and contribution from geomagnetic perturbations during the observed periods may be partly responsible for the difference.

[13] Figure 3 examines the longitudinal variation of the mean vertical and zonal drifts and their standard deviation around the magnetic equator (averaged over $\pm$10° around the magnetic equator) at all local times. The most prominent longitudinal feature in the vertical and zonal drifts and their standard deviation is the three-peak structure, especially during the daytime. This is likely caused by the strong DE2 component (Figure 1). At LT1000, the upward drift peaks at ~120°W, 0 and 120°E, while the westward drift peaks are ~50° eastward of the upward drift peaks. The local time and longitudes of the vertical drift peaks are in general agreement with those obtained by ROCSAT-1 for November–February of 1999–2002 [*Kil et al*., 2008], although the latter also shows a maximum near 170°W. The standard deviation has three maximums around local noon, and they are about 20°west of the vertical drift peaks. Standard deviation of vertical drift exceeding 10 $ms^{-1}$ is found around dawn between 30–80°W (American sector) and 40–60°E, and dusk between 80 and 130°W. The standard deviation of the equatorial zonal drift is 10–15 $ms^{-1}$ during the day at most longitudes, with a notable minimum in the American sector and two shallower minima around 60°E and 180°E/W. The largest standard deviation of the equatorial zonal drift (>20 $ms^{-1}$) is found between LT0-LT0400 and 110–70°W, LT2000–2300 and 70°$W$ – 10°E, and around LT2200 and 90°E.

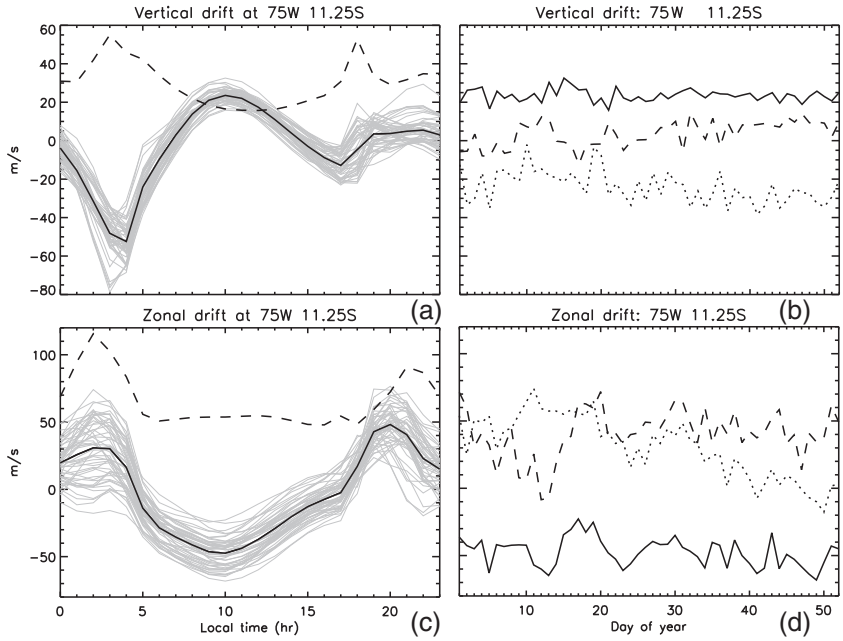


**Figure 2.** (a) The vertical $E \times B$ drift at 11.25°S/75°W from each day of the simulation (gray), the mean value (black solid), and the standard deviation (dashed, multiplied by 5). (b) Time series of the vertical drift at LT0500 (dotted), LT1000 (solid), and LT1900 (dashed). (c) Similar to (a), but for zonal $E \times B$ drift. (d) Similar to (b), but for zonal drift at LT0200 (dotted), LT1000 (solid), and LT2100 (dashed).

[14] The variability in winds and plasma drifts causes plasma density variability through transport. Figures 4a–c shows the F2 peak electron densities (NmF2) and their standard deviation at three locations from the model simulation. At 51.25°N/0° longitude, the mean NmF2 reaches the maximum value of $3.3\times10^{11}$m$^{-3}$ around LT1100, and the early morning/nighttime values are around $10^{11}$ m$^{-3}$. The scattering around the mean value is $\pm6\times10^{10}$ m$^{-3}$ around noon and about $\pm3\times10^{10}$ m$^{-3}$ during early morning/nighttime (on average ±20% and ±30%, respectively). The standard deviation is $3\times10^{10}$ m$^{-3}$ during the day and $1–2\times10^{10}$ m$^{-3}$ during early morning/nighttime (10% and 10–20%, respectively). At the geographic equator and 75°W (near the northern branch of the EIA peak), the maximum NmF2 is $8.5\times10^{11}$ m$^{-3}$ and occurs at LT1400. The variability is strongest in the afternoon, with maximum scattering ($\pm3\times10^{11}$ m$^{-3}$) and standard deviation ($1.5\times10^{11}$ m$^{-3}$) at LT1600, corresponding to ±46% and 23% of mean NmF2 value at this time. The relative variability at nighttime is also very large. At 51.25°S/57.5°W, the NmF2 peak is at LT1400, and strongest variability is around LT1500 (scattering of $\pm10^{10}$ m$^{-3}$ and standard deviation of $5\times10^{10}$ m$^{-3}$, or ±30% and 15% of the mean value).

[15] As shown by *Rishbeth and Mendillo* [2001], the NmF2 measured over Slough (52°N/1°W) display a scattering of ~±40% and 20% relative standard deviation during the day under solar minimum conditions for December/January. These values are about twice as large as those from the model simulations at a similar location (Figure 4a). As pointed out by *Rishbeth and Mendillo* [2001], meteorological and geomagnetic forcing may contribute comparably to the day-to-day variability, and the latter is not included in the simulations presented here. The daily maximum NmF2 over Port Stanley (52°S/58°W) shows a scattering

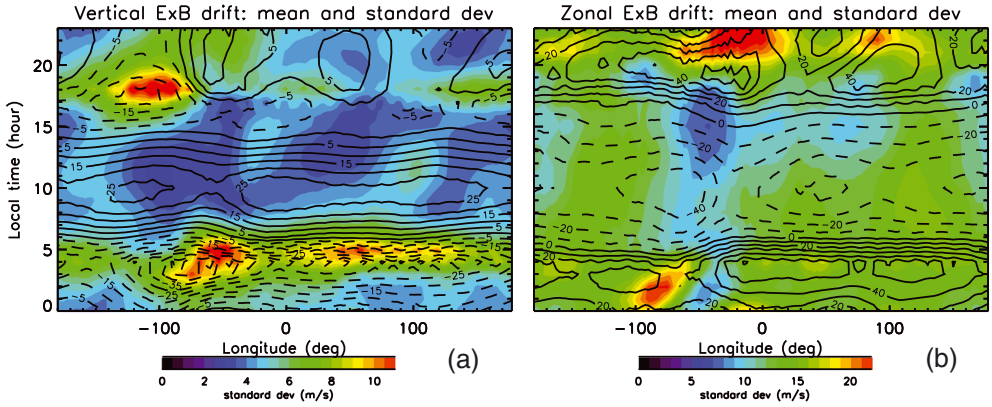


**Figure 3.** The mean (lines) and standard deviation (shades) of (a) vertical drift and (b) zonal drift, averaged over ±10° around the magnetic equator. Solid contour lines: (a) upward; (b) eastward. Contour intervals: (a) 5 ms$^{-1}$; (b) 10 ms$^{-1}$.

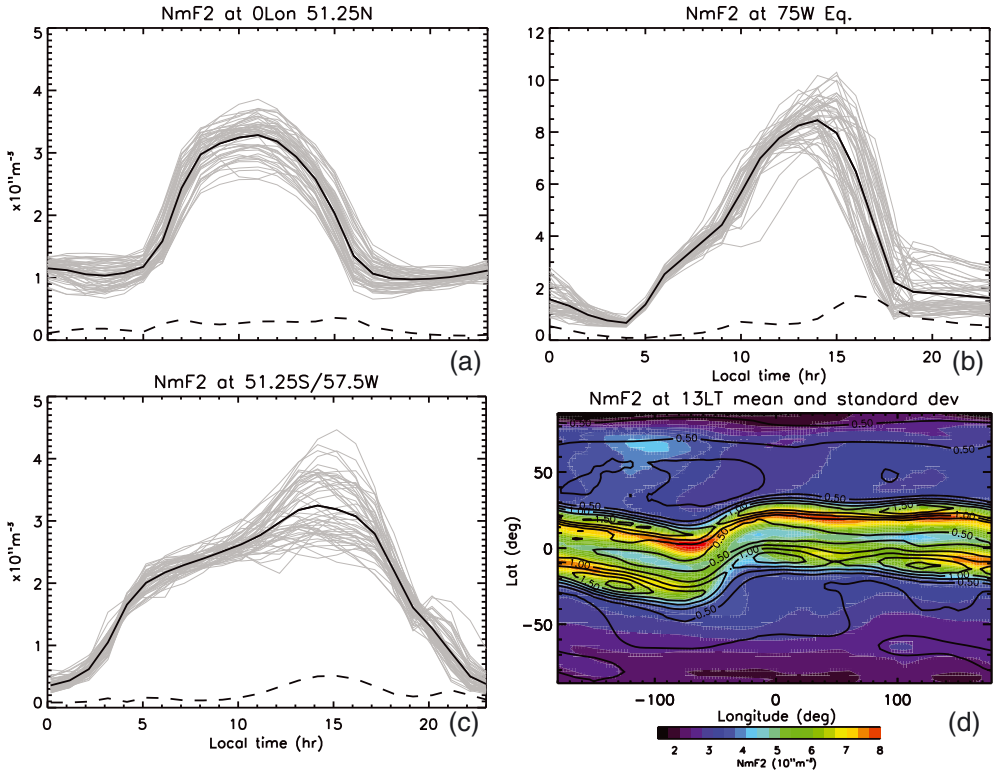


**Figure 4.** Daily values of NmF2 (gray), their mean values (black solid), and the standard deviation (dashed) for (a) 51.25°N/0 longitude, (b) equator/75°W, and (c) 51.25°S/57.5°W (all geographic). (d) Mean values (shades) and standard deviation (lines) of NmF2 for LT1300. Contour intervals: $2.5\times10^{10}$ $m^{-3}$.

of ~±20% over days 10–60 of 2002 (solar maximum) [*Rishbeth*, 2006]. This is smaller than the relative NmF2 variability from this simulation (under solar minimum conditions). The TIME-GCM simulation with its lower boundary specified by NCAR-NCEP reanalysis, on the other hand, only produces a scattering of ±3–5% [*Rishbeth*, 2006]. Day-to-day variability of NmF2 is also clearly seen in the supplementary animation of the simulation results.

[16] The longitude/latitude structure of NmF2 and its standard deviation at LT1300 clearly show a three-peak structure of the EIA. The peaks in EIA are located at or around 120°W/E and 0 longitude, in general agreement with the peaks of the vertical drift (Figure 3a). It should be noted that, however, the peaks are not symmetric with respect to the magnetic equator (generally larger north of the magnetic equator), and their geographic longitudes are not the same. The largest standard deviations are found at the same latitudes as the EIA peaks, although their longitudinal locations do not exactly coincide. The three-peak structure is observed in the topside plasma by ROCSAT-1 for January–February 1999–2002 [*Kil et al.*, 2008]. The locations of the three peaks from the simulation are in general agreement with the observation, although the plasma density in the observation shows more symmetry with respect to the magnetic equator.

## 4. Summary and Conclusions

[17] A novel approach to incorporate the weather dynamics of the LA from WACCM-X/MERRA simulations into the TIME-GCM was introduced to investigate the atmosphere-ionosphere coupling. The new scheme can provide more realistic LA driving than lower boundary specification for studying the IT variability. A January–February 2006 simulation has been performed using TIME-GCM with the constraining scheme under constant solar minimum and geomagnetically quiet conditions. The mean zonal wind, migrating, and nonmigrating tides in the thermosphere from the simulation show large day-to-day variability, with the standard deviation of DW1, DE2, and DE3 being 50% of their respective mean amplitudes, and standard deviation of SW2 25% of its mean amplitude in the lower thermosphere/E region. The mean vertical and zonal $E \times B$ drifts from the simulation are in general agreement with climatology for December–February under solar minimum conditions, except at local night when the model underestimates the downward drift and eastward drift. The vertical and zonal drifts and the F2 peak plasma density (NmF2) show longitude variations with a three-peak structure, especially during daytime, which are likely caused by the dominant DE2 during January–February. The model also produces remarkable day-to-day variability in vertical and zonal $E \times B$ drifts and NmF2, much stronger than previous model results with boundary specification by daily or 6-hourly reanalysis data. The standard deviations of the drifts and NmF2 from the model show clear local time and longitudinal dependence that are consistent with observations. The magnitudes of the standard deviation are 50% or more of those obtained from observations, consistent with the finding by *Rishbeth and Mendillo* [2001] that the meteorological driving may contribute comparably with geomagnetic forcing to the IT day-to-day variability. It should be emphasized that the IT variability in the model results exclusively from the LA driving because the solar and geomagnetic activities

are kept constant and low throughout the simulation. We thus demonstrate that the meteorological driving plays a key role in IT day-to-day variability and space weather.

[18] **Acknowledgments.** This work is in part supported by National Science Foundation grant AGS-1138784 and NASA LWS NNX08AQ91G. The National Center for Atmospheric Research is sponsored by the National Science Foundation.

## References

Akmaev, R. A. (2011), Whole atmosphere modeling: Connecting terrestrial and space weather, *Rev. Geophys.*, *49*, RG4004, doi:10.1029/2011RG000364.

Chau, J. L., L. P. Goncharenko, B. G. Fejer, and H.-L. Liu (2012), Equatorial and low latitude ionospheric effects during sudden stratospheric warming events. Ionospheric effects during SSW events, *Space Sci. Rev.*, *168*, 385–417, doi:10.1007/s11214-011-9797-5.

Fejer, B. G., and L. Scherliess (2001), On the variability of equatorial f-region vertical plasma drifts, *J. Atmos. Solar Terr. Phys.*, *63*, 893–897.

Fejer, B. G., J. R. Souza, A. S. Santos, and A. E. Costa Pereira (2005), Climatology of F region zonal plasma drifts over Jicamarca, *J. Geophys. Res.*, *110*, A12310, doi:10.1029/2005JA011324.

Fuller-Rowell, T. J., H. Wang, R. A. Akmaev, F. Wu, T.-W. Fang, M. Iredell, and A. D. Richmond (2011), Forecasting the dynamic and electrodynamic response to the January 2009 sudden stratospheric warming, *Geophys. Res. Lett.*, *38*, L13102, doi:10.1029/2011GL047732.

Immel, T. J., E. Sagawa, S. L. England, S. B. Henderson, M. E. Hagan, S. B. Mende, H. U. Frey, C. M. Swenson, and L. J. Paxton (2006), Control of equatorial ionospheric morphology by atmospheric tides, *Geophys. Res. Lett.*, *33*, doi:10.1029/2006GL026161.

Jin, H., Y. Miyoshi, D. Pancheva, P. Mukhtarov, H. Fujiwara, and H. Shinagawa (2012), Response of migrating tides to the stratospheric sudden warming in 2009 and their effects on the ionosphere studied by a whole atmosphere-ionosphere model GAIA with COSMIC and TIMED/SABER observations, *J. Geophys. Res.*, *117*, A10323, doi:10.1029/2012JA017650.

Kil, H., E. R. Talaat, S.-J. Oh, L. J. Paxton, S. L. England, and S.-Y. Su (2008), Wave structures of the plasma density and vertical E × B drift in low-latitude F region, *J. Geophys. Res.*, *113*, A09312, doi:10.1029/2008JA013106.

Liu, H.-L. (2013), WACCM-X simulation of upper atmosphere wave variability, in *Modeling the Ionosphere and Thermosphere System*, edited by J. Huba, R. Schunk, and G. Khazanov, Geophysical Monograph Series, Americal Geophysical Union, doi:10.1029/2012GM001338, in press.

Liu, H.-L., F. Sassi, and R. R. Garcia (2009), Error growth in a whole atmosphere climate model, *J. Atmos. Sci.*, *66*, 173–186.

Liu, H.-L., et al. (2010), Thermosphere extension of the whole atmosphere community climate model, *J. Geophys. Res.*, *115*, A12302, doi:10.1029/2010JA015586.

Richmond, A. D., E. C. Ridley, and R. G. Roble (1992), A thermosphere/ionosphere general circulation model with coupled electrodynamics, *Geophys. Res. Lett.*, *19*, 601–604.

Rienecker, M. M., et al. (2011), MERRA: NASA's Modern-Era Retrospective Analysis for Research and Applications, *J. Clim.*, *24*, 3624–3648, doi:10.1175/JCLI-D-11-00015.1.

Rishbeth, H. (2006), F-region links with the lower atmosphere?, *J. Atmos. Solar Terr. Phys.*, *68*, 469–478.

Rishbeth, H., and M. Mendillo (2001), Patterns of ionospheric variability, *J. Atmos. Solar Terr. Phys.*, *63*, 1661–1680.

Roble, R. G. (2000), On the feasibility of developing a global atmospheric model extending from the ground to the exosphere, in *Atmospheric Science Across the Stratopause*, edited by D. E. Siskind, S. D. Eckermann, and M. E. Summers, no. 123 in Geophysical Monograph Series, p. 342, Americal Geophysical Union.

Sagawa, E., T. J. Immel, H. U. Frey, and S. B. Mende (2005), Longitudinal structure of the equatorial anomaly in the nighttime ionosphere observed by IMAGE/FUV, *J. Geophys. Res.*, *110*, A11302, doi:10.1029/2004JA010848.

Scherliess, L., and B. G. Fejer (1999), Radar and satellite global equatorial F region vertical drift model, *J. Geophys. Res.*, *104*, 6829–6842.